Video Article

Preparation of Authigenic Pyrite from Methane-bearing Sediments for *In Situ* Sulfur Isotope Analysis Using SIMS

Zhiyong Lin[1,3], Xiaoming Sun[1,2,3,4], Jörn Peckmann[5], Yang Lu[2,3], Harald Strauss[6], Li Xu[2,3], Hongfeng Lu[7], Barbara M.A. Teichert[6]

[1]School of Earth Sciences and Engineering, Sun Yat-sen University

[2]School of Marine Sciences, Sun Yat-sen University

[3]Guangdong Provincial Key Laboratory of Marine Resources and Coastal Engineering

[4]South China Sea Bio-Resource Exploitation and Utilization Collaborative Innovation Center

[5]Institut für Geologie, Universität Hamburg

[6]Institut für Geologie und Paläontologie, Westfälische Wilhelms-Universität Münster

[7]Guangzhou Marine Geological Survey

Correspondence to: Xiaoming Sun at eessxm@mail.sysu.edu.cn

URL: https://www.jove.com/video/55970
DOI: doi:10.3791/55970

Keywords: Environmental Sciences, Issue 126, Sulfur isotopes, SIMS, pyrite, sediment, seepage, sulfate-driven anaerobic oxidation of methane, anaerobic oxidation

Date Published: 8/31/2017

Citation: Lin, Z., Sun, X., Peckmann, J., Lu, Y., Strauss, H., Xu, L., Lu, H., Teichert, B.M. Preparation of Authigenic Pyrite from Methane-bearing Sediments for *In Situ* Sulfur Isotope Analysis Using SIMS. *J. Vis. Exp.* (126), e55970, doi:10.3791/55970 (2017).

Abstract

Different sulfur isotope compositions of authigenic pyrite typically result from the sulfate-driven anaerobic oxidation of methane (SO_4-AOM) and organiclastic sulfate reduction (OSR) in marine sediments. However, unravelling the complex pyritization sequence is a challenge because of the coexistence of different sequentially formed pyrite phases. This manuscript describes a sample preparation procedure that enables the use of secondary ion mass spectroscopy (SIMS) to obtain *in situ* $\delta^{34}S$ values of various pyrite generations. This allows researchers to constrain how SO_4-AOM affects pyritization in methane-bearing sediments. SIMS analysis revealed an extreme range in $\delta^{34}S$ values, spanning from -41.6 to +114.8‰, which is much wider than the range of $\delta^{34}S$ values obtained by the traditional bulk sulfur isotope analysis of the same samples. Pyrite in the shallow sediment mainly consists of ^{34}S-depleted framboids, suggesting early diagenetic formation by OSR. Deeper in the sediment, more pyrite occurs as overgrowths and euhedral crystals, which display much higher SIMS $\delta^{34}S$ values than the framboids. Such ^{34}S-enriched pyrite is related to enhanced SO_4-AOM at the sulfate-methane transition zone, postdating OSR. High-resolution *in situ* SIMS sulfur isotope analyses allow for the reconstruction of the pyritization processes, which cannot be resolved by bulk sulfur isotope analysis.

Video Link

The video component of this article can be found at https://www.jove.com/video/55970/

Introduction

Methane emissions from sediments are common along continental margins[1,2]. However, most of the methane in areas of diffusive seepage is oxidized at the expense of sulfate within the sediments, a process known as SO_4-AOM (Equation 1)[3,4]. The production of sulfide during this process commonly results in the precipitation of pyrite. Also, OSR also drives the formation of pyrite by releasing sulfide (Equation 2)[5].

$$CH_4 + SO_4^{2-} \rightarrow HS^- + HCO_3^- + H_2O \quad (1)$$

$$2CH_2O + SO_4^{2-} \rightarrow H_2S + 2HCO_3^- \quad (2)$$

It has been found that authigenic sulfide in the sulfate-methane transition zone (SMTZ) reveals high $\delta^{34}S$ values, which was suggested to be caused by enhanced SO_4-AOM in areas of seepage[6,7,8]. In contrast, pyrite induced by OSR commonly displays lower $\delta^{34}S$ values[9]. However, it is challenging to identify different pyrite generations induced by these processes (*i.e.,* OSR and SO_4-AOM) if only a bulk sulfur isotope measurement is used, since the successively formed interfingering pyrite generations are characterized by different isotopic compositions. Therefore, microscale *in situ* sulfur isotope analysis is required to improve our understanding of the actual mineralizing processes[10,11,12].
As a versatile technique for *in situ* isotope analysis, SIMS requires only a few nanograms of sample, which sparked its designation as a nondestructive technique. A primary ion beam sputters the target, causing the emission of secondary ions that are subsequently transported to a mass spectrometer for measuring[13]. In an early *in situ* sulfur isotope analysis application of SIMS, Pimminger *et al.* successfully analyzed the $\delta^{34}S$ values in galena by using a 10 - 30 µm-diameter beam[14]. This approach has been increasingly applied to the microanalysis of sulfur isotopic compositions in sulfides, with significant improvements in both measurement precision and resolution[11,12,13,14,15,16,17,18,19,20]. Pyrite with various morphologic attributes and distinct sulfur stable isotope patterns has been reported from seep and non-seep environments[21,22,23,24].

However, to the best of our knowledge, prior to our recent SIMS study[6], only one study used the *in situ* sulfur isotope analysis of pyrite from seep environments and revealed large sulfur isotope variability in biogenic pyrite[25].

In this study, we applied SIMS to analyze the $\delta^{34}S$ values of different generations of authigenic pyrite from a seepage site in the South China Sea, which allowed for microscale discrimination of OSR- and SO_4-AOM-derived pyrite.

Protocol

1. Collection of Samples from a Sediment Core

Note: The core HS148 was obtained from a site near the gas hydrate drilling zone in the Shenhu area, South China Sea, during a cruise of the R/V Haiyang Sihao in 2006.

1. Cut the piston core (here, HS148) into sections at intervals of 0.7 m from the top to the bottom (onboard the vessel) and transfer the sections to a cold room (4 °C) for storage after retrieval.
2. Transfer the core sections to a cold room (4 °C) in the land-based lab for storage after the cruise. Take the sections out of the cold room and use a saw to cut them into halves lengthwise.
3. Clean the surface of the sediment and collect a set of sediment samples (15 cm in length; 1/4 of the sediment core) across the entire length using a knife. Pack the wet samples individually in zippered plastic bags and label them using a marker.
4. Place the wet sediment samples (~30 g) in pre-cleaned beakers and dry them at 40 °C in a drying oven for 24 h. After drying, separate the sediments into two aliquots: one for the collection of pyrite aggregates (*i.e.,* authigenic pyrite), and the other for bulk sulfur extraction (see step 3).
5. Put one aliquot of dry sediment into beakers and add distilled water to soften the sediment for 2 h. Transfer the slurry (including the sediments and water in the beaker) to a 0.063-mm sieve washed with distilled water.
    1. Sift the sediment with distilled water so that all fine grains (<0.063 mm) are washed through. Collect the coarse fraction (*e.g.*, quartz grains, fossil shells, and authigenic minerals) in beakers and dry them at 40 °C in a drying oven for 24 h.
6. Place some of the coarse segment fractions on a glass slide under a binocular microscope (20X magnification). Identify the pyrite aggregates from the coarse fraction. Handpick such pyrite aggregates using a needle and pack them individually into zippered plastic bags.
   NOTE: Most of the pyrite aggregates are black in color and tubular in shape.
7. Pulverize a second aliquot of dry sediment sample into a fine powder (<0.074 mm) using an agate mortar for further bulk sulfur extraction (see step 3).

2. Observation of Variable Morphologies

1. Select some representative pyrite tubes from the handpicked pyrite aggregates under a binocular microscope (20X magnification) for thick section preparation to examine the morphological and textural features of the pyrite aggregates.
2. Stick double-sided tape on a slide and place the selected pyrite tubes on the tape. Put a mounting tube (25 mm in diameter) on the slide to cover all pyrite aggregates. Mix 10 mL of epoxy resin with 1.3 mL of hardener at room temperature and pour the mixing liquid into the mounting tube.
    1. Place the slide and the mounting tube into a vacuum chamber. Pump the air out of the chamber until the pressure in the chamber is below 0.2 bar, so that all the pore spaces of the samples are filled with epoxy. Move the slide and the mounting tube out of the chamber and let the epoxy cure at room temperature for 12 h.
    2. After the epoxy has cured, hand-grind the pyrite tubes on a fixed, 9-μm diamond mesh pad until the pyrite grains are exposed. Hand-polish the pyrite grains to produce a smooth and flat surface, using 5-, 3-, and 1-μm diamonds successively.
3. Observe the morphology and the texture of the pyrite under a reflected light microscope at 200X magnification, with a ~3-mm working distance.
4. Perform petrographic observation under a reflected light microscope[6] and then coat the thick sections with a 25-nm layer of carbon. Examine their morphological and textural features using a thermal field emission scanning electron microscope with secondary electron imaging and backscattered electron modes[6,19].
   NOTE: This step was performed at the School of Earth Science and Geological Engineering, Sun Yat-sen University.

3. Bulk Sulfur Isotope Analyses

Note: The total sulfur (as sulfide) was extracted as hydrogen sulfide *via* wet chemical sequential extraction[26,27] at the Institut für Geologie und Paläontologie, Westfälische Wilhelms-Universität Münster.

1. Place 4 g of the dried sample powder or 10 mg of pyrite aggregates per flask into round-bottom flasks and add 10 mL of ethanol into each flask as a catalyst.
    1. Prepare zinc acetate (3%) acetic acid solution in a 500-mL glass flask to trap hydrogen sulfide. Connect the zinc acetate-containing flask to the sample-containing flask. Check the connections of the flasks and flush nitrogen into the flasks to remove the air.
2. Inject 20 mL of HCl solution (25%) into the round-bottom flasks using a syringe to liberate the acid-volatile (mono)sulfides (AVS) from the sample; allow the samples to react for 1 h at room temperature.
   NOTE: Here, the analysis revealed that no AVS was present in the studied samples.
3. Inject 30 mL of 1 M $CrCl_2$ solution into the round-bottom flasks when the above reaction is completed; allow the samples to react for 2 h at 85 °C.

NOTE: Chromium reducible sulfur (CRS, pyrite) reduces to hydrogen sulfide (H_2S) after the reaction and precipitates as zinc sulfide in the zinc acetate trap.

4. Transfer all the solutions containing zinc sulfide precipitates to beakers and convert the zinc sulfide precipitates to silver sulfide (Ag_2S) by adding a 0.1 M $AgNO_3$ solution to the beakers. Place the beakers on the heating plate and heat them to 90 °C so that the finely disseminated Ag_2S better coagulates.
    1. Collect the Ag_2S precipitates by filtration (<0.45 µm) after the solution has cooled down to room temperature and dry the filtrate overnight at 40 °C.

5. Weigh 200 µg of Ag_2S precipitate and mix it with an equal amount of V_2O_5 in tin cups. Have the sulfur composition analyzed on SO_2 molecules via combustion using a mass spectrometer connected to an elemental analyzer (EA-IRMS)[6].
NOTE: The above step was performed at the Institut für Geologie und Paläontologie, Westfälische Wilhelms-Universität Münster.

4. *In Situ* SIMS Analysis

1. Select representative pyrite aggregates with characterized crystal habits (*e.g.,* framboids, overgrows, and euhedral crystals) from different sediment samples after petrographic study. Stick the selected pyrite aggregates and pieces of Sonora pyrite standard to double-sided tape. Mold them within 5 mm of the center of a 25-mm epoxy mount.
NOTE: The epoxy disc production process is the same as in step 2.2.
    1. After the epoxy has cured, hand-grind the disc on a fixed 9-µm diamond mesh pad to the desired level so that pyrite grains are exposed. Hand-polish the epoxy discs to produce a smooth, flat surface, successively using 5-, 3-, and 1-µm diamonds, which is required for high-precision isotope ratio analysis by SIMS[28].

2. Clean the surface of the epoxy disc with deionized water and ethanol. Place the epoxy disc in a gold-coating machine and coat the dry surface sections with a 25-nm layer of gold.
    1. Observe the sample again under a scanning electron microscope at 1,000X magnification, with a 9-mm working distance, to select spots characterized with different crystal habits (*e.g.,* framboids, overgrows, and euhedral crystals) for SIMS analysis.
    NOTE: High-spatial resolution SIMS sulfur isotope analysis was applied to reveal the sulfur isotope variability of the different pyrite types.

3. Perform SIMS analysis[15,16].
NOTE: Performed at the SIMS lab of the Guangzhou Institute of Geochemistry, Chinese Academy of Sciences.
    1. Use a Cs^+ primary ion beam to measure the sulfur isotope ratios ($^{34}S/^{32}S$) of pyrite. Focus the Cs^+ primary ion beam onto a 15 µm × 10 µm spot at an energy of 10 kV, with 2.5-nA current. Use three off-axis Faraday cups for the simultaneous measurement of ^{32}S, ^{33}S, and ^{34}S in multi-collector mode, with an entrance slit width of 60 µm and an exit slit width of 500 µm on each of the three Faraday cup detectors.

4. Carry out sulfur isotope analyses in automated sequences, with each analysis consisting of 30 s of pre-sputtering, 60 s of secondary ion automated centering, and 160 s of data acquisition and sulfur isotope signal integration (40 cycles × 4 s).
    1. Analyze Sonora pyrite as a standard at regular intervals, every 5 - 6 sample analyses.
    NOTE: See Chen *et al.*[19] for more detailed analytical methods and instrument parameters.

Representative Results

Data Expression - Bulk Sulfur Isotopes:

The bulk sulfur isotope ratio is expressed in relation to the Vienna Canyon Diablo Troilite (V-CDT) standard, and the analytical precision is better than ±0.3‰. The sulfur isotope measurements were calibrated with international reference materials: IAEA-S1 ($\delta^{34}S$ = -0.30‰), IAEA-S2 ($\delta^{34}S$ = -21.55‰), IAEA-S3 ($\delta^{34}S$ = -31.4‰), and NBS 127 ($\delta^{34}S$ = 20.30‰).

$$\delta^{34}S\ (‰, \text{V-CDT}) = \left[\left(\frac{\left(^{34}S/^{32}S\right)_{sample}}{\left(^{34}S/^{32}S\right)_{\text{V-CDT}}}\right) - 1\right] \times 1{,}000$$

Data Expression - SIMS Sulfur Isotopes:

Measured ratios of $^{34}S/^{32}S$ from SIMS analyses are normalized using the V-CDT standard and are calculated as "raw" $\delta^{34}S$ values following standard delta notation:

$$\delta^{34}S_{raw}\ (‰, \text{V-CDT}) = \left[\left(\frac{\left(^{34}S/^{32}S\right)_{raw}}{\left(^{34}S/^{32}S\right)_{\text{V-CDT}}}\right) - 1\right] \times 1{,}000$$

The correction factor (α) of the instrumental bias of the $\delta^{34}S$ values for pyrite measurements was calculated using the $\delta^{34}S_{raw}$ values of the bracketing analyses of Sonora pyrite[17] ($\delta^{34}S$= +1.61‰), as follows:

$$\alpha = \frac{1+\left(\frac{\delta^{34}S_{raw}}{1,000}\right)}{1+\left(\frac{\delta^{34}S_{sonora}}{1,000}\right)}$$

The $\delta^{34}S$ values of the samples are calibrated with the measured $\delta^{34}S$ values and the correction factor (α), as follows:

$$\delta^{34}S_{sample}\ (‰, \text{V-CDT}) = 1,000 \times \left[\frac{1+\frac{\delta^{34}S_{raw}}{1,000}}{\alpha} - 1\right].$$

Outcomes:

Most pyrite aggregates hand-picked from the sediment are black in color and tubular in shape, varying from 3 to 8 mm in length and 0.2 to 0.6 mm in diameter (**Figure 1**). The pyrite aggregates mainly consist of three types of pyrite, with different morphologies: (1) framboids, (2) overgrowth layers surrounding the framboidal cores, and (3) euhedral crystals. In the shallow sediment above a depth of 483 cmbsf, most pyrite occurs as framboids, while overgrowth layers and euhedral crystals become abundant at greater depths, reflecting a change of pyrite crystal habits with depth (**Figure 2**).

The total CRS content ranges from 0.0 wt.% to 0.98 wt.% (n = 29). Below 50 cmbsf, it exhibits minor fluctuations around the mean value (0.44 wt.%) and two distinct peaks of 0.98 wt.% at 490 cmbsf and 0.78 wt.% at 590 cmbsf[6] (**Table 1** and **Figure 3A**). The $\delta^{34}S_{CRS}$ values fall between -40.5 and +41.0‰ (n = 28), and the $\delta^{34}S_{py}$ values of hand-picked pyrite range from -37.6 to +52.7‰ (n = 28)[6] (**Figure 3B**). Above 483 cmbsf, both $\delta^{34}S_{CRS}$ and $\delta^{34}S_{py}$ values display a similar trend, reflecting an almost linear increase with depth. Further down, two distinctly different groups of $\delta^{34}S_{CRS}$ values are observed, one reflecting a notable ^{34}S depletion, with values between -34 and -27‰, and a second group with high $\delta^{34}S_{CRS}$ values, ranging from -8 to +41‰. In contrast, all hand-picked pyrite aggregates exhibit exclusively positive $\delta^{34}S$ values (> +20‰), revealing ^{34}S enrichment compared to total sulfide sulfur (up to 75‰) (**Figure 3B**).

Pyrite aggregates from site HS148 display extremely variable *in situ* $\delta^{34}S$ values, between -41.6 and +114.8‰ (n = 81), reflecting an overall range of 156.4‰[6] (**Table 2** and **Figure 3B**). These SIMS data reveal a similar down core trend, like the $\delta^{34}S$ values of CRS and of pyrite aggregates. CRS and pyrite aggregates are subsumed and referred to as bulk pyrite below. Above 500 cmbsf, both *in situ* and bulk pyrite $\delta^{34}S$ values reflect ^{34}S depletion (as low as -41.6‰). With increasing depth (below 500 cmbsf), the SIMS $\delta^{34}S$ values reveal extreme ^{34}S enrichment (up to +114.8‰), while the highest $\delta^{34}S$ value of bulk pyrite only reaches +52.7‰. Moreover, all overgrowths and euhedral crystals show higher $\delta^{34}S$ values than bulk pyrite, while most of the framboids display lower $\delta^{34}S$ values. The $\delta^{34}S$ values in different types of pyrite revealed a variability of more than 100‰ in single-pyrite tubes.

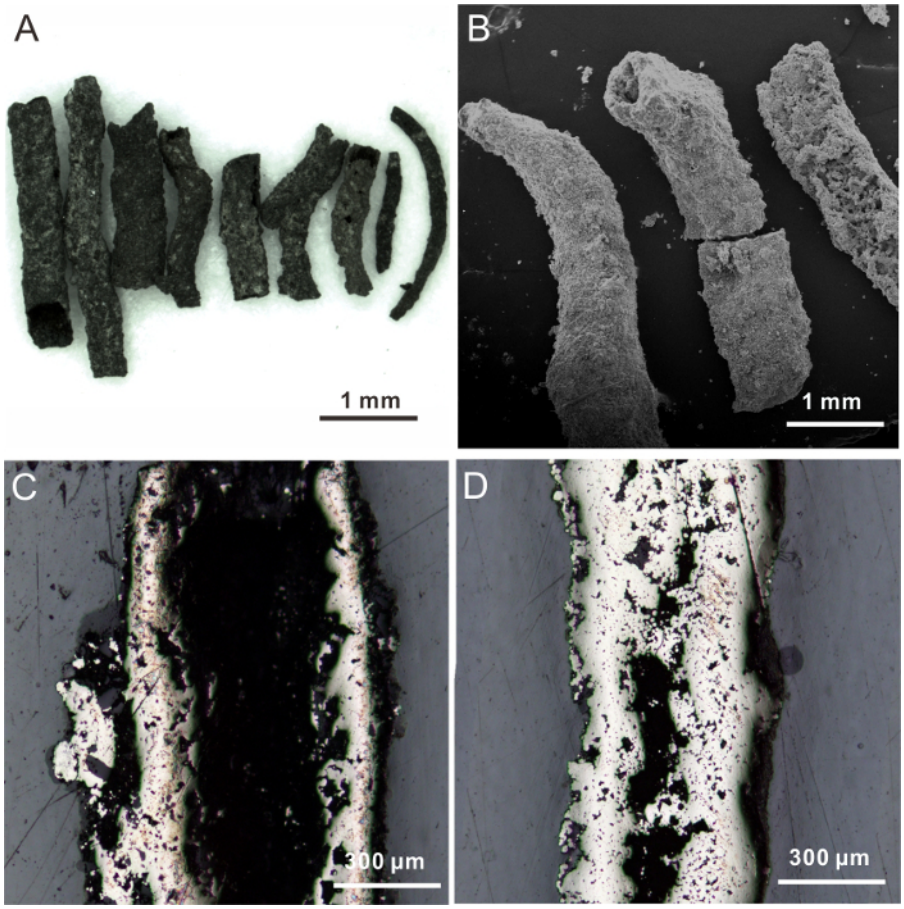

Figure 1. Typical Morphologies of Authigenic Pyrite. (A) Pyrite tubes of various sizes, taken from sediments. **(B)** Pyrite tubes; SEM micrograph. **(C and D)** Longitudinal cross-sections of pyrite tubes, with hollow interiors and different wall thicknesses; reflected-light photographs. This figure has been modified from Lin *et al.*[6]. Please click here to view a larger version of this figure.

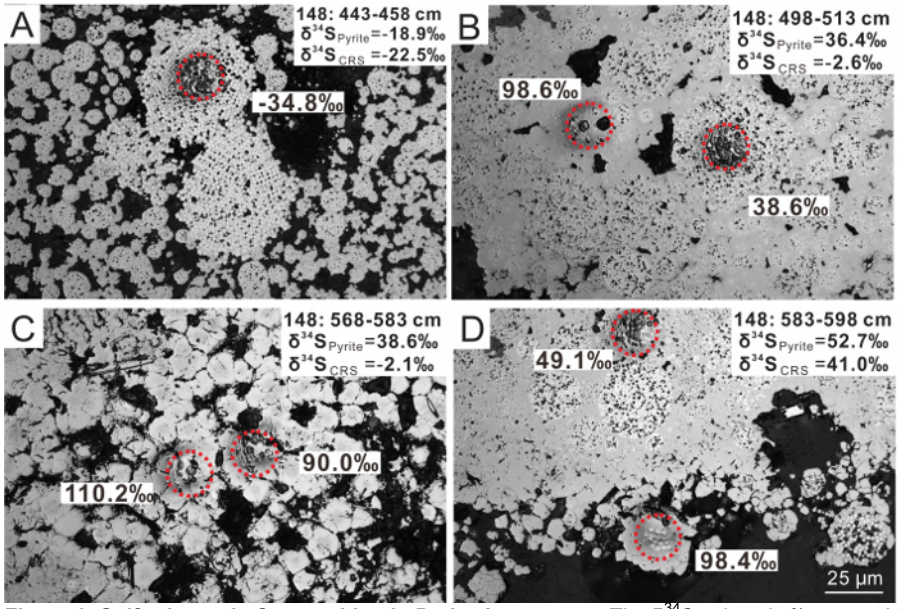

Figure 2. Sulfur Isotopic Composition in Pyrite Aggregates. The $\delta^{34}S$ values in ‰ versus V-CDT were analyzed by secondary ion mass spectrometry; corresponding spot locations are indicated on the reflected-light photomicrographs (see the red circles). **(A-D)** Typical pyrite aggregates, from shallow to deep sediments. Most of the pyrite in **(A)** is framboidal and depleted in ^{34}S, while overgrowths and euhedral crystals enriched in ^{34}S are abundant in **(B-D)**. The scale provided in **(D)** is the same for all micrographs. This figure has been modified from Lin *et al.*[6]. Please click here to view a larger version of this figure.

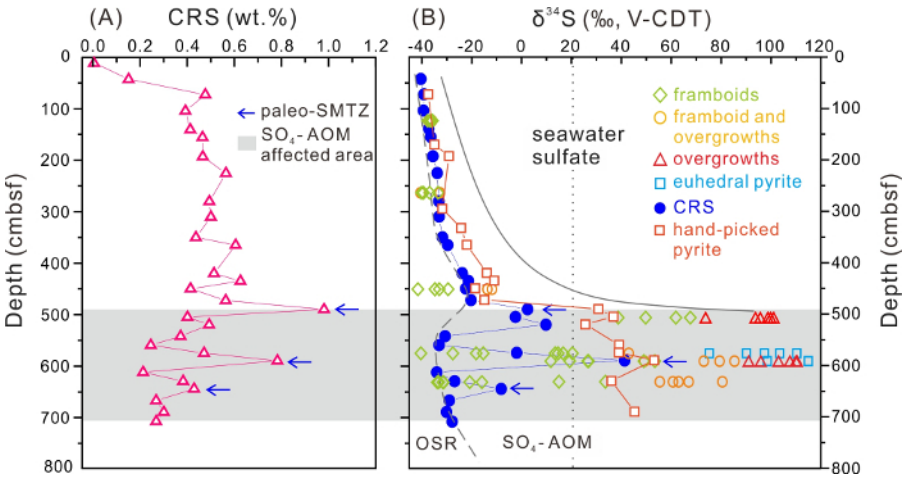

Figure 3. The Content and Sulfur Isotopic Compositions of Sulfide Minerals at Site HS148. (A) CRS content; **(B)** SIMS $\delta^{34}S$ values of the three types of pyrite and $\delta^{34}S$ values of CRS and hand-picked pyrite aggregates. The dashed line separates a zone to the left, suggested to be dominated by OSR, and a zone to the right, suggested to be dominated by SO_4-AOM. The shaded area refers to the zone affected by SO_4-AOM. This figure has been modified from Lin *et al.*[6]. Please click here to view a larger version of this figure.

Depth (cmbsf)	CRS (wt.%)	$\delta^{34}S_{CRS}$ (‰ V-CDT)	$\delta^{34}S_{pyrite}$ (‰ V-CDT)
0-20	0	-	-
35-50	0.15	-40.5	-
65-80	0.48	-39.3	-37.6
95-113	0.39	-39.4	-
113-133	-	-	-
133-148	0.41	-37.3	-
148-163	0.46	-36.5	-
163-178	-	-	-35.2
183-203	0.47	-35.6	-29.4
218-233	0.56	-33.9	-
253-273	-	-	-
273-288	0.49	-33.2	-
288-303	-	-	-32
303-318	0.5	-33.2	-
323-343	-	-	-24.5
343-358	0.44	-31.8	-
358-373	0.6	-29.7	-22.2
393-413	-	-	-
413-428	0.51	-23.9	-14.2
428-443	0.63	-21.5	-11.3
443-458	0.41	-22.5	-18.9
463-483	0.56	-20.4	-15.2
483-498	0.98	2.2	30.4
498-513	0.4	-2.6	36.4
513-528	0.49	9.5	25.2
533-553	0.37	-30.7	-
553-568	0.24	-33.2	38.7
568-583	0.47	-2.1	38.6
583-598	0.78	41	52.7
603-623	0.21	-34.1	-
623-638	0.38	-26.9	35.6
638-653	0.43	-8.3	-
653-668	0.27	-29.1	-
683-698	0.3	-30.2	44.9
699-719	0.27	-28	-

Table 1. Content of the CRS and Sulfur Isotopic Composition. Content of the CRS and sulfur isotopic composition of CRS and pooled, hand-picked samples of pyrite at site HS148[6].

Depth (cmbsf)	$\delta^{34}S$ (‰ V-CDT)	2SD	Pyrite type
113-133	-35.9	0.1	F
113-133	-37.4	0.1	F+O
113-133	-36	0.13	F
113-133	-37.3	0.07	F+O
113-133	-36.6	0.11	F
113-133	-35.9	0.11	F
113-133	-36.8	0.1	F
113-133	-37.7	0.13	F
113-133	-36.1	0.02	F+O
113-133	-35.9	0.11	F
113-133	-36	0.1	F+O
113-133	-35.8	0.12	F
253-273	-39.4	0.12	F
253-273	-40.6	0.03	F+O
253-273	-33.6	0.09	F
253-273	-40.1	0.14	F
253-273	-32.7	0.17	F+O
253-273	-33	0.08	F+O
253-273	-36.9	0.08	F
443-458	-33	0.11	F
443-458	-34.8	0.1	F
443-458	-41.6	0.05	F
443-458	-34.8	0.15	F
443-458	-11.9	0.25	F+O
443-458	-29.5	0.05	F
443-458	-13.8	0.23	F+O
498-513	38.6	0.35	F
498-513	98.6	0.26	O
498-513	67.5	0.09	F
498-513	99.6	0.15	O
498-513	93.6	0.25	O
498-513	95.5	0.02	O
498-513	49.6	0.19	F
498-513	100.8	0.06	O
498-513	61.7	0.08	F
498-513	73.6	0.2	O
568-583	110.2	0.04	E
568-583	90	0.19	E
568-583	97.1	0.27	E
568-583	75.1	0.2	E
568-583	-27.7	0.07	F
568-583	42.8	0.23	O
568-583	103.3	0.16	E
568-583	13.3	0.32	F

568-583	-15.5	0.18	F
568-583	-40.5	0.02	F
568-583	20.3	0.15	F
568-583	-18.4	0.06	F
568-583	16.5	0.1	F
568-583	14.5	0.18	F
583-598	107.4	0.16	O
583-598	26.8	0.17	F
583-598	100.6	0.14	O
583-598	95.8	0.14	O
583-598	90.9	0.02	O
583-598	85.2	0.46	F+O
583-598	79.2	0.07	F+O
583-598	103.8	0.3	O
583-598	53.3	0.26	F
583-598	48.9	0.15	F
583-598	114.8	0.32	E
583-598	109.9	0.45	O
583-598	72.9	0.23	F+O
583-598	11.6	0.1	F
583-598	19.2	0.3	F
583-598	49.1	0.18	F+O
583-598	26.4	0.45	F
583-598	110.3	0.4	O
623-638	66.9	0.23	F+O
623-638	80.3	0.03	F+O
623-638	55.3	0.24	F+O
623-638	14.9	0.24	F
623-638	33.5	0.12	F
623-638	62.8	0.04	F+O
623-638	60.5	0.29	F+O
623-638	-31.4	0.04	F
623-638	-33.7	0.03	F
623-638	-20.6	0.05	F
623-638	-15.9	0.03	F
623-638	-31.5	0.12	F
623-638	-33.2	0.12	F
Uncertainty for $\delta^{34}S$ is 2SD (standard deviation).			

Table 2. *In Situ* Sulfur Isotopic Composition of Different Types of Pyrite. *In situ* sulfur isotopic composition of different types of pyrite, analyzed by secondary ion mass spectrometry at site HS148. F = framboid, O = overgrowth, E = euhedral crystal, F+O = mixture of framboid and overgrowth[6].

Discussion

The sulfur isotope analysis of pyrite is a useful approach and can help in identifying the biogeochemical processes that impact pyritization. However, if bulk sulfur isotope analysis is applied, the obtained sulfur isotope signatures commonly represent mixed signals, as sedimentary pyrite aggregates typically consist of multiple, closely interfingering generations. Here, we present a method (*i.e.,* SIMS analysis) for analyzing the *in situ* sulfur isotopic compositions of various pyrite generations on the micro-scale. The critical steps within this protocol include: (1) the

selection of well-characterized pyrite generations from different sediment depths (*e.g.,* framboids, overgrowths, and euhedral grains); (2) the identification of pyrite aggregates large enough (> 20 µm) for SIMS analysis, to avoid the mixing of different paragenetic phases; and (3) the analysis of a sufficient number of spots (*i.e.,* at least 10 spots per sample, if possible), to ensure that the obtained isotope patterns are representative, reflecting the environmental conditions during pyrite formation.

In this study, we applied SIMS to analyze the *in situ* $\delta^{34}S$ values of various pyrite generations with different morphologies, including framboids, overgrowths, and euhedral grains. In addition, the bulk $\delta^{34}S$ values of the total CRS and hand-picked pyrite aggregates (> 0.063 mm) in the sediment were also determined for comparison. It is obvious that the SIMS $\delta^{34}S$ values cover a much wider range (from -41.6 to +114.8‰) than those of bulk pyrite. From the SIMS analysis, it becomes apparent that ^{34}S-depleted framboids are particularly abundant in the shallow sediment (*i.e.,* above 483 cmbsf), which is also recorded by the ^{34}S depletion of bulk pyrite. Such sulfur isotope patterns indicate that OSR is the dominant diagenetic process in the shallow sediment in the study area[6,9].

With increasing depth (*i.e.,* below 483 cmbsf), both *in situ* and bulk pyrite analyses yielded high $\delta^{34}S$ values, including extremely high SIMS $\delta^{34}S$ values (as high as +114.8‰). It is interesting to note that some individual zones, with the synchronous increase of the CRS content and $\delta^{34}S_{CRS}$ value, can be identified throughout the sediment column (see the arrows in **Figure 3**). Such a synchronous increase is attributed to the formation of progressively ^{34}S-enriched hydrogen sulfide during SO_4-AOM in a paleo-SMTZ[6,8,23]. Moreover, below 483 cmbsf, the SIMS $\delta^{34}S$ values of radial overgrowths and euhedral crystals are systematically higher than those of framboids. The increase in $\delta^{34}S$ values along a transect from the framboidal core to the overgrowth layers and euhedral crystals within individual pyrite aggregates is best explained by the subsequent growth of later pyrite generations derived from SO_4-AOM over initial framboids derived from OSR at shallower depths[6]. Such great variability in the $\delta^{34}S$ values of different pyrite generations reveals a complex diagenetic history of pyritization, which cannot be resolved by traditional bulk sulfur isotope analysis.

SIMS is a versatile technique for *in situ* isotope analysis, but some factors still limit its wider application. For example, it is challenging, if not impossible, to apply SIMS to minerals with a crystal diameter that is smaller than the spatial resolution of this method (~10 µm)[15,16]. Also, SIMS can only be used to analyze the isotopic composition of a mineral if a corresponding mineral standard (the same mineral with a known isotopic composition) is available[14,15].

In our study of authigenic pyrite from methane-bearing sediments, high-spatial resolution SIMS analysis proved its potential to distinguish the effects of OSR and SO_4-AOM on pyritization. This analytical approach can serve as a sensitive tool for reconstructing the pyritization sequence that developed during diagenesis in marine sediments. Future applications of this protocol should also target ancient sedimentary sequences, aiming to resolve the effects of different biogeochemical processes on mineral formation when pore water data is lacking.

Disclosures

The authors have nothing to disclose.

Acknowledgements

This research was jointly funded and supported by the Natural Science Foundation of China (No. 91128101, 41273054, and 41373007), the China Geological Survey Project for South China Sea Gas Hydrate Resource Exploration (No. DD20160211), Fundamental Research Funds for the Central Universities (No. 16lgjc11), and Guangdong Province Universities and Colleges Pearl River Scholar Funded Scheme (No. 2011). Zhiyong Lin acknowledges the financial support provided by the China Scholarship Council (No. 201506380046). Yang Lu thanks the Guangzhou Elite Project (No. JY201223) and the China Postdoctoral Science Foundation (No. 2016M592565). We are grateful to Dr. Shengxiong Yang, Guangxue Zhang, and Dr. Jinqiang Liang of the Guangzhou Marine Geological Survey for providing samples and valuable suggestions. We thank Dr. Xianhua Li and Dr. Lei Chen of the Institute of Geology and Geophysics (Beijing), Chinese Academy of Sciences, for help with the SIMS analysis. Dr. Xiaoping Xia is thanked for making available the SIMS Lab of the Guangzhou Institute of Geochemistry, Chinese Academy of Sciences, for the filming of this article. The manuscript benefited from comments from Dr. Alisha Dsouza, review editor of JoVE, and two anonymous referees.

References

1. Judd, A.G. The global importance and context of methane escape from the seabed. *Geo-Mar Lett.* **23**, 147-154 (2003).
2. Suess, E. Marine cold seeps and their manifestations: geological control, biogeochemical criteria and environmental conditions. *Int J Earth Sci.* **103**, 1889-1916 (2014).
3. Boetius, A. *et al.* A marine microbial consortium apparently mediating anaerobic oxidation of methane. *Nature.* **407**, 623-626 (2000).
4. Orphan, V. J., House, C. H., Hinrichs, K.-U., McKeegan, K. D., DeLong, E. F. Methane-consuming archaea revealed by directly coupled isotopic and phylogenetic analysis. *Science.* **293** (5529), 484-487 (2001).
5. Jørgensen, B. B. Mineralization of organic matter in the seabed - the role of sulfate reduction. *Nature.* **296**, 643-645 (1982).
6. Lin, Z. Y. *et al.* How sulfate-driven anaerobic oxidation of methane affects the sulfur isotopic composition of pyrite: A SIMS study from the South China Sea. *Chem Geol.* **440**, 26-41 (2016).
7. Jørgensen, B. B., Böttcher, M. E., Lüschen, H., Neretin, L. N., Volkov, I. I. Anaerobic methane oxidation and a deep H_2S sink generate isotopically heavy sulfides in Black Sea sediments. *Geochim Cosmochim Ac.* **68** (9), 2095-2118 (2004).
8. Borowski, W. S., Rodriguez, N. M., Paull, C. K., Ussler, III. W. Are ^{34}S-enriched authigenic sulfide minerals a proxy for elevated methane flux and gas hydrates in the geologic record? *Mar Petrol Geol.* **43**, 381-395 (2013).
9. Canfield, D. E. Isotope fractionation by natural populations of sulfate-reducing bacteria. *Geochim Cosmochim Ac.* **65** (7), 1117-1124 (2001).
10. McKibben, M.A., Eldridge, C.S. Micron-scale isotopic zoning in minerals; a record of large-scale geologic processes. *Mineral Mag.* **58A**, 587-588 (1994).

11. Peevler, J., Fayek, M., Misra, K. C., Riciputi, L. R. Sulfur isotope microanalysis of sphalerite by SIMS: constraints on the genesis of Mississippi valley-type mineralization, from the Mascot-Jefferson City district, East Tennessee. *J Geochem Explor.* **80** (2-3), 277-296 (2003).
12. Ferrini, V., Fayek, M., De Vito, C., Mignardi, S., Pignatti, J. Extreme sulphur isotope fractionation in the deep Cretaceous biosphere. *J Geol Soc.* **167**, 1009-1018 (2010).
13. Ireland, T.R. *et al.* Charge-mode electrometer measurements of S-isotopic compositions on SHRIMP-SI. *Int J Mass Spectrom.* **359** (1), 26-37 (2014).
14. Pimminger, A., Grasserbauer, M., Schroll, E., Cerny, I. Microanalysis in galena by Secondary Ion Mass Spectrometry for determination of sulfur isotopes. *Anal Chem.* **56** (3), 407-411 (1984).
15. Eldridge, C. S., Compston, W., Williams, I. S., Walshe, J. L., Both, R. A., In situ microanalysis for $^{34}S/^{32}S$ ratios using the ion microprobe SHRIMP. *Int J Mass Spectrom Ion Processes.* **76** (1), 65-83 (1987).
16. Kozdon, R., Kita, N. T., Huberty, J. M., Fournelle, J. H., Johnson, C. A., Valley, J. W. In situ sulfur isotope analysis of sulfide minerals by SIMS: precision and accuracy, with application to thermometry of 3.5 Ga Pilbara cherts. *Chem Geol.* **275** (3-4), 243-253 (2010).
17. Farquhar, J. *et al.* Pathways for Neoarchean pyrite formation constrained by mass-independent sulfur isotopes. *Proc Natl Acad Sci USA.* **110** (44), 17638-17643 (2013).
18. Whitehouse, M. Multiple sulfur isotope determination by SIMS: evaluation of reference sulfides for $\Delta^{33}S$ with observations and a case study on the determination of $\Delta^{36}S$. *Geostand Geoanal Res.* **37** (1), 19-33 (2013).
19. Chen, L. *et al.* Extreme variation of sulfur isotopic compositions in pyrite from the Qiuling sediment-hosted gold deposit, West Qinling orogen, central China: an in situ SIMS study with implications for the source of sulfur. *Miner Depos.* **50** (6), 643-656 (2015).
20. LaFlamme, C. *et al.* In situ multiple sulfur isotope analysis by SIMS of pyrite, chalcopyrite, pyrrhotite, and pentlandite to refine magmatic ore genetic models. *Chem Geol.* **444**, 1-15 (2016).
21. Peckmann, J. *et al.* Methane-derived carbonates and authigenic pyrite from the northwestern Black Sea. *Mar Geol.* **177**, 129-150 (2001).
22. Zhang, M. *et al.* Morphology and formation mechanism of pyrite induced by the anaerobic oxidation of methane from the continental slope of the NE South China Sea. *J Asian Earth Sci.* **92**, 293-301 (2014).
23. Lin, Z. Y. *et al.* Stable isotope patterns of coexisting pyrite and gypsum indicating variable methane flow at a seep site of the Shenhu area, South China Sea. *J Asian Earth Sci.* **123**, 213-223 (2016).
24. Virtaslo, J. J. *et al.* Pyritic and baritic burrows and microbial filaments in postglacial lacustrine clays in the northern Baltic Sea. *J Geol Soc London.* **167** (6), 1185-1198 (2010).
25. Kohn, M. J., Riciputi, L. R., Stakes, D., Orange, D. L. Sulfur isotope variability in biogenic pyrite: Reflections of heterogeneous bacterial colonization? *Am Mineral.* **83** (11-12, Part 2) (1998).
26. Canfield, D. E., Raiswell, R., Westrich, J. T., Reaves, C. M., Berner, R. A. The use of chromium reduction in the analysis of reduced inorganic sulfur in sediments and shales. *Chem Geol.* **54**, 149-155 (1986).
27. Rice, C. A., Tuttle, M. L., Reynolds, R. L. The analysis of forms of sulfur in ancient sediments and sedimentary rocks: comments and cautions. *Chem Geol.* **107** (1-2), 83-95 (1993).
28. Kita, N. T., Huberty, J. M., Kozdon, R., Beard, B. L., Valley, J. W. High-precision SIMS oxygen, sulfur and iron stable isotope analyses of geological materials: accuracy, surface topography and crystal orientation. *Surf Interface Anal.* ***43*** .(1-2), 427-431 (2011).

